

Technical Note

Spatial and Temporal Variation Patterns of NO 5.3 μm Infrared Radiation during Two Consecutive Auroral Disturbances

Fan Wu ^{1,2,3} , Congming Dai ^{2,3,*} , Shunping Chen ^{2,3}, Cong Zhang ^{2,3}, Wentao Lian ^{1,2,3}  and Heli Wei ^{2,3} 

¹ School of Environmental Science and Optoelectronic Technology, University of Science and Technology of China, Hefei 230026, China; lwentao@mail.ustc.edu.cn (W.L.)

² Key Laboratory of Atmospheric Optics, Anhui Institute of Optics and Fine Mechanics, Hefei Institutes of Physical Science (HFIPS), Chinese Academy of Sciences, Hefei 230031, China; hlwei@aiofm.ac.cn (H.W.)

³ Advanced Laser Technology Laboratory of Anhui Province, Hefei 230037, China

* Correspondence: cmdai@aiofm.ac.cn

Abstract: The variation in key parameters of the solar–terrestrial space during two consecutive auroral disturbances (the magnetic storm index, Dst index = -422 nT) that occurred during the 18–23 November 2003 period was analyzed in this paper, as well as the spatiotemporal characteristics of NO 5.3 μm radiation with an altitude around the location of 55°N 160°W . The altitude was divided into four regions (50–100 km, 100–150 km, 150–200 km, and 200–250 km), and it was found that the greatest amplification occurs at the altitude of 200–250 km. However, the radiance reached a maximum of 3.38×10^{-3} W/m²/sr at the altitude of 123 km during the aurora event, which was approximately 10 times higher than the usual value during “quiet periods”. Based on these findings, the spatiotemporal variations in NO 5.3 μm radiance within the range of latitude 51°S – 83°N and longitude of 60°W – 160°W were analyzed at 120 km, revealing an asymmetry between the northern and southern hemispheres during the recovery period. Additionally, the recovery was also influenced by the superposition of a second auroral event. The data used in this study were obtained from the OMNI database and the SABER (Sounding of the Atmosphere using Broadband Emission Radiometry) infrared radiometer onboard the TIMED (Thermosphere-Ionosphere-Mesosphere Energetics and Dynamics) satellite. Finally, the correlation of NO 5.3 μm radiance at 120 km with temperature, solar wind speed, auroral electrojet index (AE index), and Dst index were analyzed. It was found that only the Dst index had a good correlation with the radiance value. Furthermore, the correlation between the Dst index and radiance at different altitudes was also analyzed, and the highest correlation was found at 170 km.

Keywords: infrared radiation; aurora; geomagnetic storm



Citation: Wu, F.; Dai, C.; Chen, S.; Zhang, C.; Lian, W.; Wei, H. Spatial and Temporal Variation Patterns of NO 5.3 μm Infrared Radiation during Two Consecutive Auroral Disturbances. *Remote Sens.* **2024**, *16*, 1420. <https://doi.org/10.3390/rs16081420>

Academic Editor: Steven Dewitte

Received: 1 March 2024

Revised: 15 April 2024

Accepted: 15 April 2024

Published: 17 April 2024



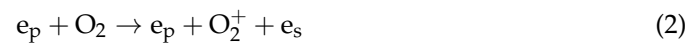
Copyright: © 2024 by the authors. Licensee MDPI, Basel, Switzerland. This article is an open access article distributed under the terms and conditions of the Creative Commons Attribution (CC BY) license (<https://creativecommons.org/licenses/by/4.0/>).

1. Introduction

The solar–terrestrial space refers to the region of space that includes the outer solar atmosphere, solar–terrestrial interplanetary space, Earth’s magnetic field, ionosphere, middle and upper atmosphere [1], which is subject to various solar activities such as sunspots and Coronal Mass Ejections (CMEs), as well as coupling among complex interactions between different parts of the solar–terrestrial space. These factors can disrupt the stability of the space environment, leading to disturbances such as geo-magnetic storms and auroras in the Earth’s space environment [2,3], and result in space weather disasters, for instance, the “Carrington event” in 1859 [4] and the collective fall of 40 SpaceX Starlink Satellites in 2022 just before reaching their designated orbit [5]. It is easy to see that the resulting space weather events can cause severe damage to space-based and ground-based systems, with profound effects on human activities [6]; therefore, there is a growing recognition of the importance of learning and warning against space weather disasters.

The aurora is a space weather phenomenon commonly observed in mid-high latitudes but can also be seen in lower latitudes during periods of intense solar activities [7,8]. The

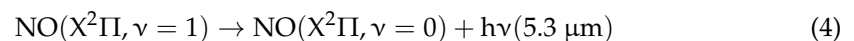
aurora originates from solar activity. During periods of increased solar activity, the solar wind, formed by the expansion of the corona, carries high-energy particles. These particles, under the influence of Earth's magnetic field, travel along magnetic field lines to the upper atmosphere above the polar regions [9]. The components of the upper atmosphere mainly include N_2 , O_2 , N and O. After the injection of auroral electrons, the neutral particles dissociate and ionize, while the auroral electrons are deposited gradually, ionizing them and generating large numbers of secondary electrons during the collision with atoms and molecules (mainly N_2 , O_2 , and N) [9], as shown by Equations (1)–(3):



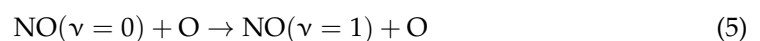
where e_p is the primary electrons and e_s is the secondary electrons. The energy of secondary electrons is small, generally below 200 eV; this energy range can cause the excitation of the electronic states of numerous molecules and atoms, but only the first generation of secondary products can be further ionized [10], which can induce electronic excitations in molecules and atoms, generating a “driving source” for subsequent photochemical reactions.

The photochemical reactions between the components are extremely complex, and the emission spectra range from extreme ultraviolet to the infrared spectral region, where the infrared band radiation accounts for more than 20% of the total emitted energy [10]. Due to their comparatively low photon energy, infrared photons usually cannot directly excite the electronic state of atoms or molecules, but rather rely on collisional excitation arising from photochemical reactions. The primary contributors to infrared radiation emissions are NO, NO^+ , and CO_2 . This paper focuses on the characteristics of 5.3 μm radiance in the aurora, where NO infrared radiation at 5.3 μm is the primary thermal equilibrium process in the atmosphere and is an important radiative cooling process in the altitude region of 110–300 km [11–13], which is known as the “natural thermostat” [14,15]. The density variation of NO is predominantly determined by latitude, longitude, altitude, and seasonal changes [16–18]. Furthermore, it is impacted by X-rays and ultraviolet radiation at low latitudes [17,19]. Specifically, under auroral conditions, the density of NO is also influenced by Joule heating and particle heating in the polar and mid-latitude regions, leading to an increase in kinetic temperature in the polar region [19–21]. During aurora and geomagnetic storm, significant amounts of energy and particles are deposited into the Earth's atmosphere, leading to alterations in its structure, composition, and dynamics. The storm energy dissipates quickly from the atmosphere, and heat balance is achieved through infrared emissions [14,22–24].

The cooling process occurs due to the conversion of kinetic energy into radiative energy, which is then released into space and the lower atmosphere [14,15]. Based on satellite observations and auroral infrared detection experiments [25–28], it has been found that during the auroral disturbance, 5.3 μm radiation mainly derives from the $\Delta v = 1$ band of NO, as shown in reaction (4):

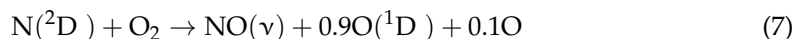


The radiation emission of NO 5.3 μm mainly results from the fundamental transition between adjacent vibrational levels. Under static atmospheric conditions, the inelastic collision between nitric oxide and atomic oxygen primarily generates this radiation [12,29,30], although N_2 and O_2 also contribute, but to a lesser extent [31]:



This reaction is a non-elastic collision process with a reaction rate of $(4.2 \times 0.7) \times 10^{-11} \exp(-2700/T) \text{ cm}^3/\text{s}$ [32,33], making it the primary source of $\text{NO}(\nu = 1)$ in the altitude regions of 110–300 km.

Under auroral disturbance conditions, in addition to the reaction (5), another main source of excited-state NO arises from collisions between O_2 and $\text{N}(^2\text{D}, ^4\text{S})$ [10,34,35]:



The rate of reaction (6) is $(1 \times 10^{-12}) \exp(-3220/T) \text{ cm}^3/\text{s}$, and the rate of reaction (7) is $(7.4 \times 10^{-12}) (T/300)^{0.5} \text{ cm}^3/\text{s}$; both are temperature-dependent.

During auroral events, the temperature of the Earth's thermosphere can increase by several hundred Kelvin due to the energy deposition, and this significant temperature rise can be effectively controlled through radiative cooling processes, as described in the reactions (4) above. Therefore, further exploration of the spatiotemporal variability in NO infrared radiation at 5.3 μm from the perspective of radiance can provide theoretical support for predicting changes in the auroral parameters caused by disturbances. On the other hand, the enhanced infrared band during an auroral disturbance serves as vital background radiation for various meteorological satellites and spacecrafts. Therefore, studying the important infrared radiation components during auroral disturbance is also crucial. In-depth analyses conducted by Mlynczak et al. [14,15] on the enhanced NO 5.3 μm infrared radiation detected by SABER in April 2002 provide a basis for studying the infrared response of thermosphere to strong disturbance events. More recently, Bag et al. [36] and Li et al. [37] investigated the asymmetry of NO 5.3 μm radiance between the Northern and Southern hemispheres and its correlation with various factors. Bag et al. [38] analyzed SABER radiation data to investigate the latitudinal and longitudinal variations in cooling rates at the NO 5.3 μm during the unusual disturbance period in 21–22 January 2005, and examined how radiation cooling rates responded to the anomalous event.

This paper includes four sections. The motivation and main purpose of this paper are briefly introduced in Section 1. The datasets used in this study are described in Section 2. The spatiotemporal variations of NO 5.3 μm radiance during auroral processes and their correlation with temperature, solar wind speed, AE index, and Dst index are mainly discussed in Section 3. Finally, we summarize the article in Section 4.

2. Data Description

2.1. Solar–Terrestrial Space Environmental Parameters

The OMNI database is a standardized collection of data on the space environment around the Earth, including solar activity and geomagnetic measurements [39,40]. The database was compiled from measurements made by multiple satellites, including ACE, WIND, IMP-8, Geotail, and ISEE-3 [40,41]. The database is available in two parts, Low-Resolution OMNI (LRO) and High-Resolution OMNI (HRO), with a high level of reliability and temporal resolution that can reach up to 1 min [42,43]. In this study, we used hourly data from the OMNI2 database for four key parameters of the space environment around the Earth during 18–23 November 2003, including the solar wind speed (V_{sm}), the north–south component of the interplanetary magnetic field (IMF B_z), the magnetic storm index (Dst index), and the auroral electrojet index (AE index). Detailed descriptions of the dataset and download instructions can be found at <https://omniweb.gsfc.nasa.gov/omniweb> (accessed on 27 August 2003).

2.2. Nitric Oxide Infrared Radiative Emission

In July 2001, NASA launched the TIMED satellite, which carried the SABER, a ten-channel broadband limb-scanning infrared radiometer, covering a spectral range of 1.27–17 μm [44]. SABER scans once every 58 s to obtain vertical profiles of atmospheric constituents, such as NO, CO_2 , O_3 , H_2O , NO, O_2 , and temperature from the surface to

an altitude of 180 km [23,45,46]. In one orbit, SABER covers latitudes from 53° in one hemisphere to 83° in the other, with an asymmetric hemispheric coverage [46–48]. SABER collects 24 h of data every 60–65 days [14,44], covering 15 longitude bands each day, and measures radiance ($\text{W}/\text{m}^2/\text{sr}$) within the tangent height range of approximately 20 to 400 km with a vertical resolution of 2 km [49]. It measures 10 emissions, including two primary coolants, NO 5.3 μm and CO₂ 15 μm [23,36,50], and measuring radiance. During the aurora period reported here, we used SABER version 2.0 data about NO 5.3 μm during 18–23 November 2003.

3. Results

3.1. The Aurora Event during 18–23 November 2003

A global severe geomagnetic storm ($\text{Dst-index} \leq -200$ nT) occurred during 18–23 November 2003, producing intense auroral events. The temporal variations in key space weather parameters such as V_{sm} , IMF B_z , Dst index, and AE index during this period are shown in Figure 1.

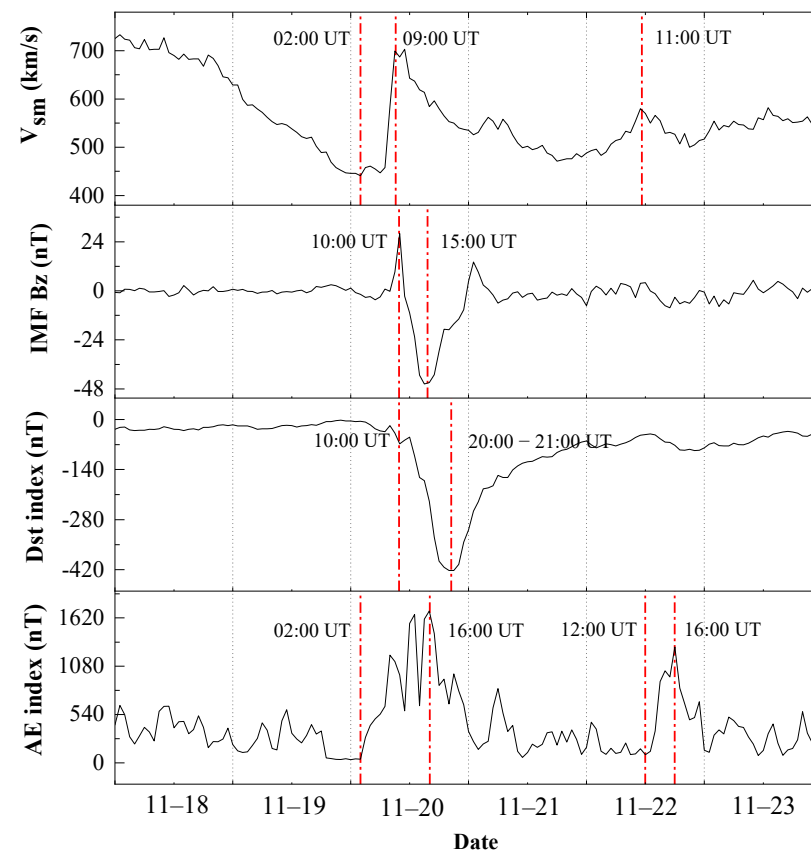


Figure 1. Temporal variations in solar wind speed V_{sm} , the interplanetary magnetic field IMF B_z , disturbance storm time index Dst, and the auroral electrojet index AE (from top to bottom) during 18–23 November 2003.

Figure 1 shows that the solar wind speed began to decrease continuously from 18 November, and reached its lowest value of 441 km/s around 02:00 UT on 20 November.

From 18 November, the solar wind speed continuously decreased and reached its lowest value of 441 km/s around 02:00 UT on 20 November, as shown in Figure 1. During this period, the IMF B_z and Dst-index remained relatively stable, while the AE index showed small fluctuations, but also remained relatively stable. Thus, the solar wind speed significantly increased and reached its first peak of 699 km/s around 09:00 UT on 20 November, carrying the IMF B_z to the Earth’s magnetosphere and reconnecting with the geomagnetic field. The high-energy particles carried by the solar wind injected into

the atmosphere along the magnetic field lines, colliding with the atoms and molecules of the upper atmosphere. This collision caused the ionization and excitation of neutral components, triggering reactions (1)–(3).

Subsequently, the Dst index rapidly decreased, marking the entry of the magnetic storm into the main phase. Within a short period, a significant change in the AE index values was observed, with an overall upward trend after fluctuating greatly from its minimum value of 40 nT around 02:00 UT on 20 November, and reaching a maximum value of 1698 nT around 16:00 UT on the same day. Within 14 h, it increased by a factor of 42, indicating the occurrence of a strong aurora [51] during this period. The IMF B_z reached its lowest value of -45.6 nT around 16:00 UT on 20 November, and the Dst index reached its lowest value of -422 nT between 20:00 UT and 21:00 UT on the same day, indicating that this was an extreme magnetic storm event [36]. Subsequently, the solar wind speed gradually decreased, signifying the entry of the magnetic storm into the recovery phase. On 23 November, the IMF B_z , Dst index, and AE index gradually returned to a quiet level. It is worth noting that at around 12:00 UT on 22 November, the AE index displayed a gradually increasing trend, reaching 1296 nT, presumably due to a small peak in the solar wind speed (580 km/s) around 11:00 UT on the same day.

3.2. Variations in Infrared Radiance at NO 5.3 μm

After determining the timing of the auroral event, we selected 32 datasets obtained from measurements performed by the SABER instrument using Channel 6. This particular channel primarily captures the NO 5.3 μm radiation. The measurements were taken at approximately 55°N 160°W , spanning around 23:00 UT on 18 November to 18:00 UT on 23 November. By employing the limb sounding technique with SABER, which integrates the measurement path radiance along the line of sight, it was evident that the majority of the radiance contribution originated from the radiation at the tangent point. Hence, we plotted the temporal variations in radiance within the altitude range of 50–250 km at the tangent point. Figure 2 illustrates the observed changes in radiance over time. Due to the transition of SABER from the “north-view” mode to the “south-view” mode on 23 November, there were no available data after 18:00 UT near this time point. Additionally, SABER provided only a single orbital measurement on 18 November, resulting in an absence of data prior to 23:00 UT.

As shown in Figure 2, the NO 5.3 μm radiance was in a quiet period during 19 November, with the average radiance value of 1.41×10^{-4} W/m²/sr throughout the entire altitude region. The radiance value first reached its peak at around 120 km altitude after 12:00 UT on 20 November due to the disturbance caused by the aurora. It then gradually extended to other altitudes and elevated upward to 250 km by 22:00 UT, with a radiation enhancement spanning 50 to 250 km. The maximum radiance across the entire altitude region reached 3.38×10^{-3} W/m²/sr at 08:00 UT on 21 November of 123 km altitude, which was about 10 times larger than the average value during quiet periods. Thereafter, the radiance outside the altitude region of 100–125 km gradually decreased, while the radiance within this range remained high. This can be attributed to the dependence of reaction rates on temperature for NO ($v = 1$) [32,52,53], despite the peak density of NO ($v = 0$) being concentrated around 105 km [19]. As a result, the radiance enhancement first appeared around 120 km and remained at a high level for about 40 h in this range. By 10:00 UT on 22 November, the entire altitude region returned to the quiet period level. However, at 18:00 UT on 22 November, the radiance suddenly increased again at around 120 km altitude and expanded within an approximately 20 km altitude region. Although the extent and intensity of this second auroral event were smaller than the first one, the radiance still reached 9.85×10^{-4} W/m²/sr at 13:00 UT on 23 November, about 7 times higher than the average value during quiet periods. This observation is consistent with the variations observed in the space environmental parameters in Figure 1, which were caused by a “little peak” in the solar wind speed on 22 November and the occurrence of a relatively weaker “secondary aurora” detected by the AE index around 16:00 UT on 23

November. Additionally, a trend of radiance recovery was observed after 17:00 UT on 23 November, despite the lack of data.

Preliminary statistical analysis was conducted on the radiance data of Figure 2 by dividing the heights equally into four altitude regions: 50–100, 100–150, 150–200, and 200–250 km. The standard deviation (STD), minimum (MIN), and maximum (MAX) values of the radiance in these four height ranges were analyzed, and the results are shown in Table 1 and the dot-line chart in Figure 3.

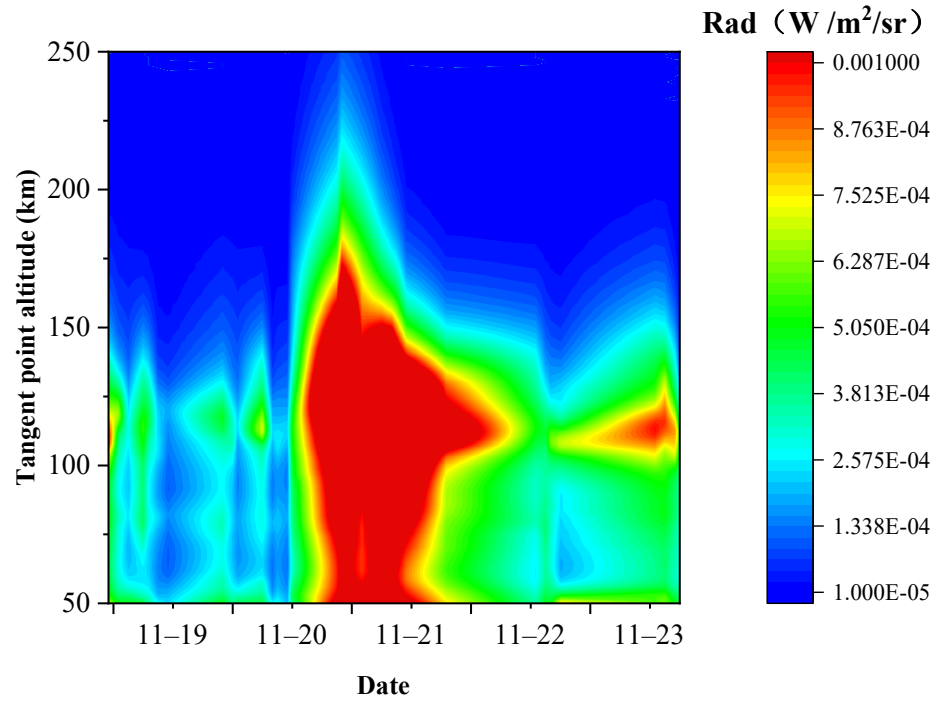


Figure 2. Variation in NO 5.3 μm radiance values over time in the altitude region of 50–250 km during 18–23 November 2003, measured by TIMED/SABER at about 55°N 160°W.

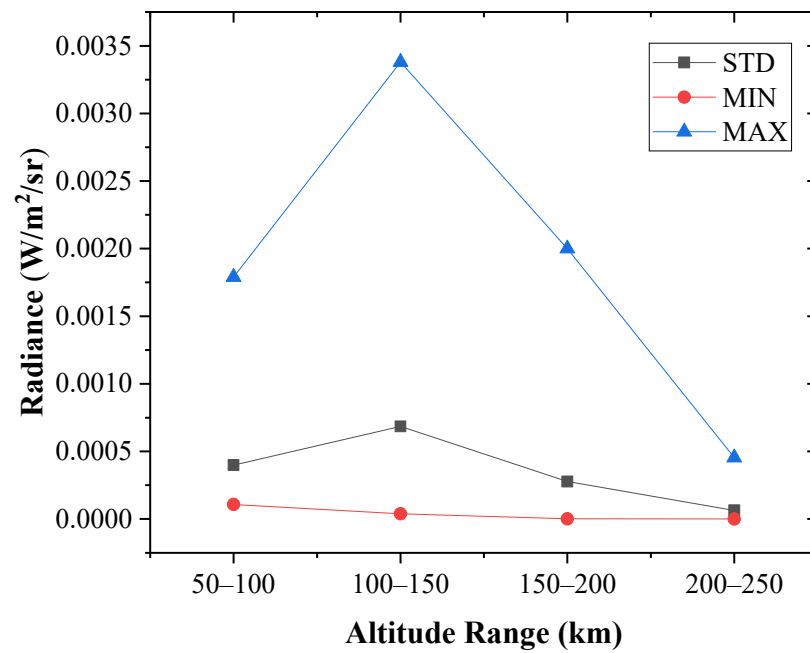


Figure 3. STD (black squares), MIN (red dots), and MAX (blue triangles) values for four different altitude regions.

Table 1. Statistical analysis of radiance in four altitude regions.

Altitude Region (km)	Statistical Value of Radiance (W/m ² /sr)		
	STD	MIN	MAX
50–100	3.99×10^{-4}	1.08×10^{-4}	1.79×10^{-3}
100–150	6.85×10^{-4}	3.81×10^{-5}	3.38×10^{-3}
150–200	2.77×10^{-4}	7.28×10^{-7}	2.00×10^{-3}
200–250	6.40×10^{-5}	1.89×10^{-9}	4.54×10^{-4}

The two charts presented above show that during the aurora event, the radiance values reach their peak at an altitude range of 100–150 km. This range exhibits a maximum value of 3.38×10^{-3} W/m²/sr and a standard deviation of 6.85×10^{-4} W/m²/sr, indicating a higher degree of variability in radiance values at these heights. The most significant amplification, however, occurs at altitudes of 200–250 km. During quiet periods, the NO 5.3 μ m radiance values in this range are considerably lower than those at other heights. Following the auroral disturbance, these values increase from 1.89×10^{-9} W/m²/sr to 4.54×10^{-4} W/m²/sr, exhibiting a difference of approximately five orders of magnitude. Notably, the maximum radiance values between altitudes of 50–200 km are approximately equal. This similarity suggests that the attainable radiance values at their maxima are constrained by temperature and particle concentration-dependent photochemical reactions.

3.3. Longitudinal and Latitudinal Distribution Characteristics of NO 5.3 μ m Limb Radiance Values at a 120 km Tangent Point Height

In order to enhance data comparability, we selected 12 orbital measurements from SABER NO 5.3 μ m radiance data taken between 18 and 23 November 2003. These measurements were taken at a tangent point height of 120 km, with a longitude ranging from 60°W to 160°W (300°–200°) and latitude from 51°S to 83°N (−51°–83°). The relevant information of the orbital measurements is presented in Table 2. Based on this, we generated a chart illustrating the variation in NO 5.3 μ m radiance value at 120 km as a function of longitude and latitude during auroral disturbances. The chart is shown in Figure 4.

Table 2. Information about the 12 selected sets of orbital data.

No.	Orbit Number	Date	Time (UT)
(a)	10,538	11-18	23:06
(b)	10,553	11-19	23:17
(c)	10,562	11-20	13:51
(d)	10,563	11-20	15:27
(e)	10,565	11-20	18:42
(f)	10,566	11-20	20:19
(g)	10,567	11-20	21:57
(h)	10,568	11-20	23:34
(i)	10,569	11-21	01:11
(j)	10,590	11-22	11:10
(k)	10,607	11-23	14:42
(l)	10,609	11-23	17:57

From Figure 4, it can be observed that the radiance values of NO 5.3 μ m in the quiet state exhibit slight fluctuations (Figure 4a,b). However, after being affected by aurora, there is an increase in radiance values in mid-high latitude regions starting from 13:51 UT on 20 November, as shown in Figure 4c. By around 21:57 UT on 20 November, the radiance values increased to a much higher level, approximately 10 times larger than the quiet state, across the entire longitude and latitude range (Figure 4g). As the disturbance recovered, the radiance values show a decreasing trend from Figure 4h to Figure 4i, and almost returned to the quiet state level by 11:10 UT on 22 November, as shown in Figure 4j. However, as seen in Figure 4k, a slight increase of approximately one order of magnitude is observed in

the radiance values in the longitude range of 200–220° and latitude range of -30° to 40° at around 13:00 UT on 23 November, which is caused by the “secondary aurora” observed at around 16:00 UT on 22 November, as shown in Figure 1. Additionally, Figure 4 illustrates the coverage of the latitude and longitude during the SABER measurements, which gradually transitioned from the “north-view” to the “south-view” mode. In Figure 4, a decrease in radiance values is observed in the range of longitude 200–220° and latitude -30° to 40° , gradually approaching the quiet state level.

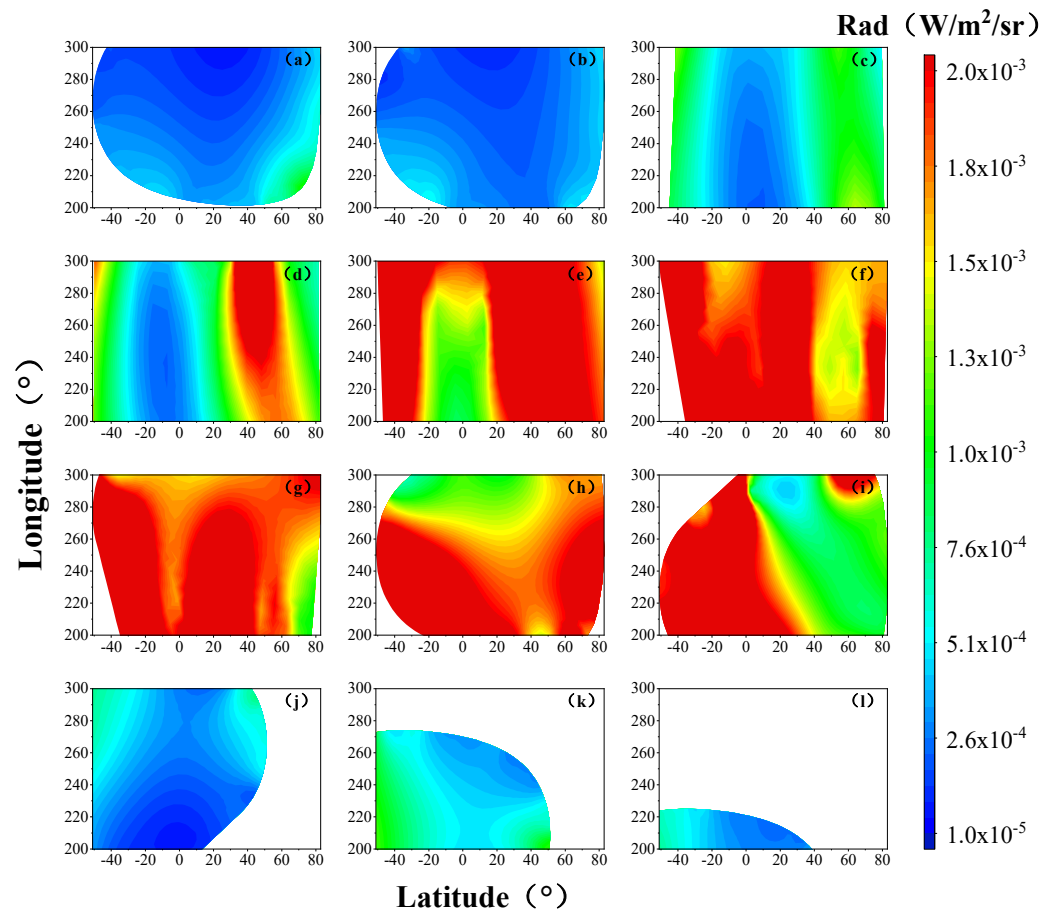


Figure 4. Longitudinal and latitudinal distribution of NO 5.3 μm radiance during 18–23 November 2003. Measurement dates and times are: (a) 11-18 23:06 UT; (b): 11-19 23:17 UT; (c): 11-20 13:51 UT; (d): 11-20 15:27 UT; (e): 11-20 18:42 UT; (f): 11-20 20:19 UT; (g): 11-20 21:57 UT; (h): 11-20 23:34 UT; (i): 11-21 01:11 UT; (j): 11-22 11:10 UT; (k): 11-23 14:42 UT; (l): 11-23 17:57 UT.

It is noteworthy that during the first “recovery phase” of radiance (Figure 4h–j), there exists a difference between the northern and southern hemispheres, with the southern hemisphere exhibiting a lag while the northern hemisphere begins the recovery process first. This phenomenon was initially attributed to the effect of coordinate system selection [54], but was refuted by Bag in 2018 and later confirmed to be influenced by the radial wind in 2021 [36].

A statistical analysis was performed on the 12 sets of NO 5.3 μm radiance values data in Figure 4, otherwise, 5 sets of orbital data with approximately the same latitude and longitude regions were included to enhance the overall understanding of the aurora process. The orbit information and statistical characteristics of each set of radiance values was shown in Table 3, including the orbit number, date, measurement time of the orbital data, mean (AVE), STD, MIN, and MAX values. These statistics are graphically represented in Figures 5 and 6 for visualization purposes. In Figure 5, the orbit number is utilized as the X-axis, with specific time information available in Table 3. In Figure 6, to enhance the

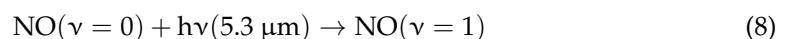
visualization of the dispersion, the 17 sets of orbital information are defined as 17 events, with each event utilized as the X-axis.

Figure 5 shows that after the aurora occurred on 20 November, as measured by orbit 10,553, the maximum radiance value increased significantly. It reached a peak of $7.91 \times 10^{-3} \text{ W/m}^2/\text{sr}$ at orbit 10,569, which is about 10 times higher than the maximum value during the quiet period. However, the minimum value showed a small increase of only $6.00 \times 10^{-4} \text{ W/m}^2/\text{sr}$ during the entire auroral disturbance. This can be attributed to the fact that the aurora only occurs within a specific range of the atmosphere, causing a greater impact on the NO 5.3 μm radiance value within that range. In contrast, the radiance change in other atmospheric regions is minimal, resulting in a more significant change in the maximum value but a minor change in the minimum value.

Table 3. Statistics values about the selected 17 groups of orbits.

Orbit Information				Statistics Values ($\text{W/m}^2/\text{sr}$)			
Number	Event	Date	Time (UT)	AVE	STD	MIN	MAX
10,538	1	11-18	23:06	3.63×10^{-4}	2.67×10^{-4}	3.24×10^{-5}	1.21×10^{-3}
10,553	2	11-19	23:17	2.87×10^{-4}	1.75×10^{-4}	3.47×10^{-5}	7.02×10^{-4}
10,562	3	11-20	13:51	9.76×10^{-4}	6.52×10^{-4}	1.79×10^{-4}	3.51×10^{-3}
10,563	4	11-20	15:27	1.42×10^{-3}	9.94×10^{-4}	2.14×10^{-4}	4.30×10^{-3}
10,565	5	11-20	18:42	2.26×10^{-3}	1.46×10^{-3}	3.78×10^{-4}	6.93×10^{-3}
10,566	6	11-20	20:19	2.16×10^{-3}	1.46×10^{-3}	3.85×10^{-4}	6.23×10^{-3}
10,567	7	11-20	21:57	2.19×10^{-3}	1.36×10^{-3}	4.55×10^{-4}	6.11×10^{-3}
10,568	8	11-20	23:34	2.19×10^{-3}	1.41×10^{-3}	4.69×10^{-4}	7.83×10^{-3}
10,569	9	11-21	01:11	2.56×10^{-3}	1.42×10^{-3}	6.39×10^{-4}	7.91×10^{-3}
10,578	10	11-21	16:10	8.43×10^{-4}	4.52×10^{-4}	2.26×10^{-4}	2.35×10^{-3}
10,588	11	11-22	08:18	4.68×10^{-4}	3.74×10^{-4}	4.64×10^{-5}	1.34×10^{-3}
10,589	12	11-22	09:56	4.52×10^{-4}	3.25×10^{-4}	6.59×10^{-5}	1.24×10^{-3}
10,590	13	11-22	11:10	4.33×10^{-4}	2.88×10^{-4}	6.68×10^{-4}	1.06×10^{-3}
10,591	14	11-22	13:12	4.12×10^{-4}	2.31×10^{-4}	1.23×10^{-4}	1.18×10^{-3}
10,593	15	11-22	16:27	4.92×10^{-4}	3.88×10^{-4}	1.13×10^{-4}	1.96×10^{-3}
10,607	16	11-23	14:42	5.68×10^{-4}	4.10×10^{-4}	1.30×10^{-4}	1.72×10^{-3}
10,609	17	11-23	17:57	5.43×10^{-4}	3.85×10^{-4}	1.37×10^{-4}	1.76×10^{-3}

It is important to note a slight decrease of approximately $1.00 \times 10^{-3} \text{ W/m}^2/\text{sr}$ in the maximum radiance value during the measurement period from orbit 10,565 to orbit 10,567. This decrease can be attributed to the temperature-controlled excitation process caused by the collision between high-energy particles carried by the solar wind and the neutral components when they reach the atmosphere. It is also influenced by the resonance absorption process of solar and terrestrial radiation described in reaction (8), as mentioned by Bharti et al. [12]. These fluctuations caused slight variations in the NO 5.3 μm radiance value within the latitude and longitude range. These variations gradually accumulated and reached their peak at orbit 10,590, before returning to the level observed during the quiet period. However, there was a slight increase again at orbit 10,607 and 10,609 due to the influence of the “secondary aurora”.



To illustrate the variability in the data dispersion, the 17 sets of measurement data were defined as 17 distinct events, and their mean and standard deviation were plotted in a dot-and-line graph with error bars (Figure 6). It can be observed from Figures 5 and 6 that the standard deviation of the NO 5.3 μm radiance values increased from 1.75×10^{-4} to $1.46 \times 10^{-3} \text{ W/m}^2/\text{sr}$ following the occurrence of the aurora. This indicates a difference of approximately one order of magnitude. The error bars in Figure 6 also reveal that the auroral disturbance had a substantial impact on the dispersion of radiance values within the specified latitude and longitude range. Specifically, it caused the dispersion to

remain at a heightened level of 1.36×10^{-3} to 1.46×10^{-3} W/m²/sr during orbit 10,565 to 10,569. These findings suggest that the limited extent of the aurora’s occurrence led to differential and lagged effects on the radiation value, resulting in increased dispersion during disturbance periods and gradual escalation to its maximum level. Upon the conclusion of the first disturbance event (orbit 10,591), the dispersion reduced to approximately 2.31×10^{-4} W/m²/sr, and subsequently witnessed a slight increase of less than one order of magnitude under the influence of the “secondary aurora”.

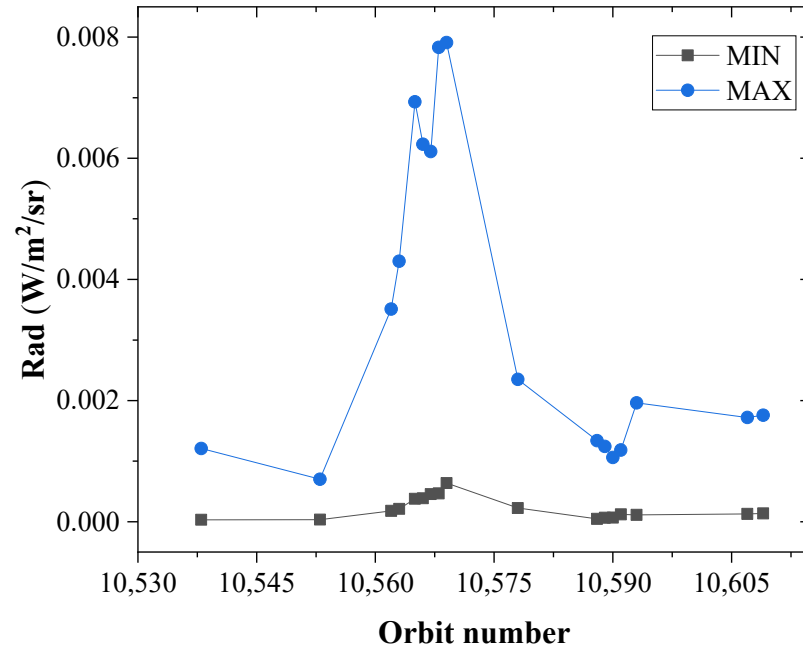


Figure 5. Variation in the maximum (blue dots) and minimum (black squares) values of NO 5.3 μm radiance for the 17 selected groups of orbits.

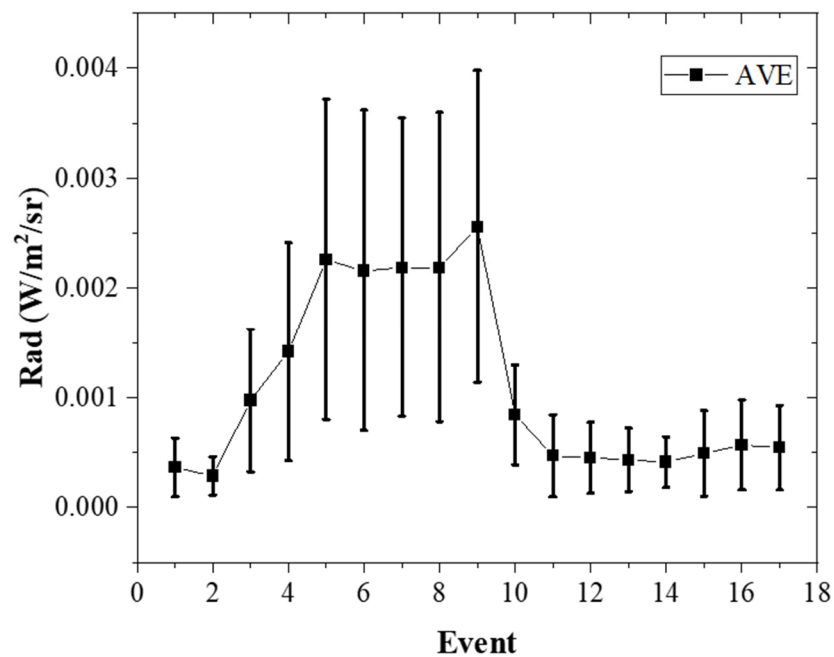


Figure 6. Variation in and values of NO 5.3 μm radiance for the 17 selected events.

3.4. Correlation Analysis between Radiance and the Dst Index during Auroral Events

Solar wind is essentially a supersonic stream of charged particles released from the outer atmosphere of the Sun during periods of strong solar activity, consisting mainly of protons and electrons. The solar wind speed, V_{sw} , is one of the most important parameters reflecting solar activity strength. The AE index is a measure of the strength of auroral electrojet currents derived from data acquired by 12 magnetometers distributed evenly along the auroral zone. On the other hand, the Dst index characterizes the intensity of symmetrical perturbations in the Earth's dipole equator magnetic field. Furthermore, the IMF B_z , displayed in Figure 1, represents the southward (northward) orientation of the interplanetary magnetic field, and it has a weak correlation with the variation in radiance. The entire radiance process at NO 5.3 μm (reactions (4)–(7)) is influenced by temperature. Hence, this study focuses on examining the correlation between radiance values measured at a distance of 120 km around 55°S 160°W of SABER channel 6 NO 5.3 μm and variables such as temperature, solar wind speed, AE index, and Dst index during the period of 18–23 November. The findings are illustrated in Figure 7, with the red line representing the fitted curve.

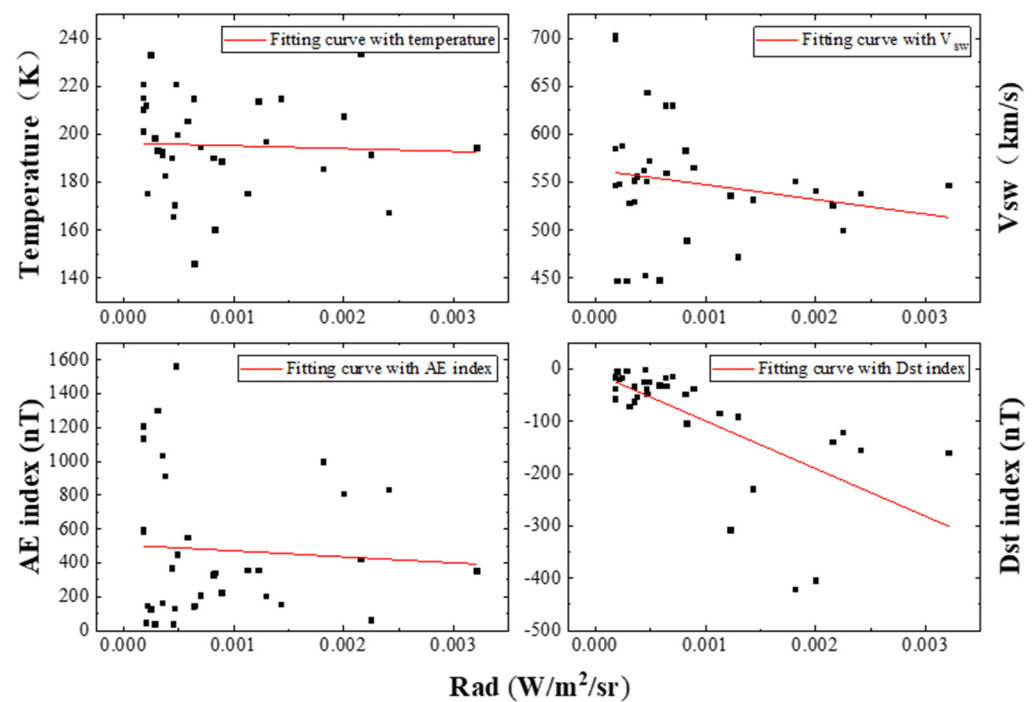


Figure 7. Correlation between the measured radiance of NO 5.3 μm at 120 km around 55°S 160°W of SABER and temperature, V_{sw} , AE index, and Dst index during 18–23 November 2003.

Figure 7 depicts a stronger correlation between the Dst index and the NO 5.3 μm radiance value, with an adjusted R^2 (R^2_{adj} , it constitutes an adjusted version of the coefficient of determination, R^2 , incorporating considerations of both the number of independent variables and the sample size to prevent overfitting) of 0.42. This could be due to reaction (4), because reaction (4) is temperature-dependent. Consequently, atmospheric parameters such as thermospheric temperature, and densities of nitric oxide and atomic oxygen dictate the behavior of nitric oxide infrared radiative emission [14,15]. These physical changes, however, are driven by changes in solar irradiance and geomagnetic conditions [24]. The Dst index directly characterizes the variations in the geomagnetic field. Hence, a significant correlation exists between them, justifying further analysis. The present study identifies the tangent point altitude with the highest correlation for the Dst index and the NO 5.3 μm radiance, and analyzes the corresponding R^2_{adj} for radiance values within the 50–200 km altitude range using a 10 km interval. These results are presented in Figures 8 and 9.

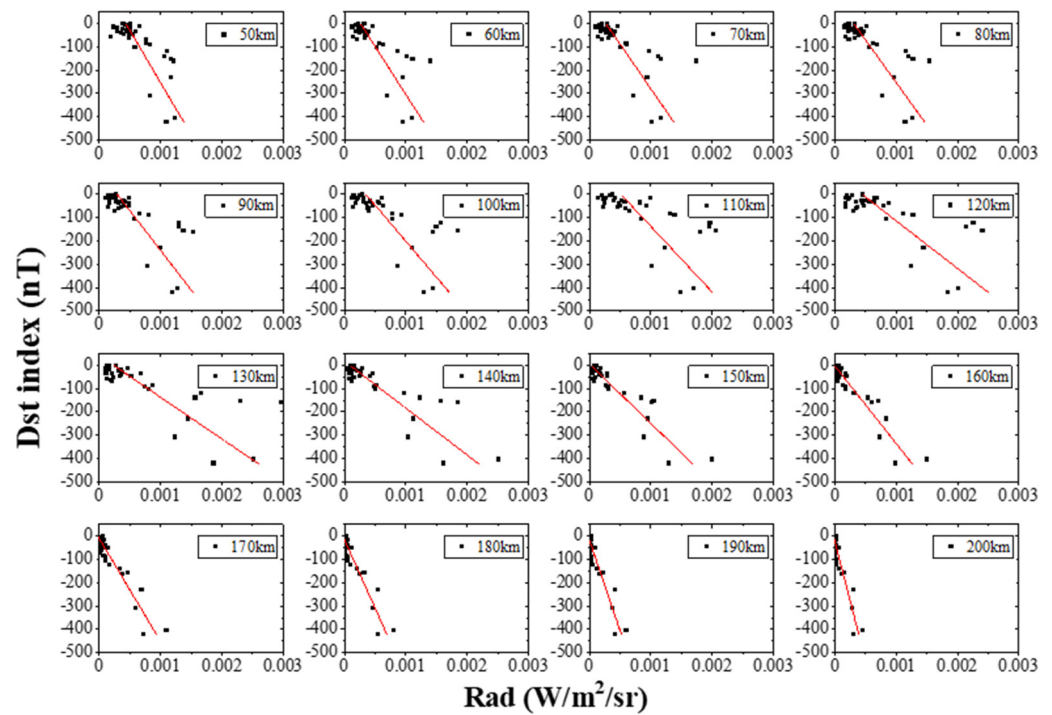


Figure 8. Correlation of Dst index with NO 5.3 μm radiance at different altitudes around 55°S 160°W of SABER during 18–23 November 2003.

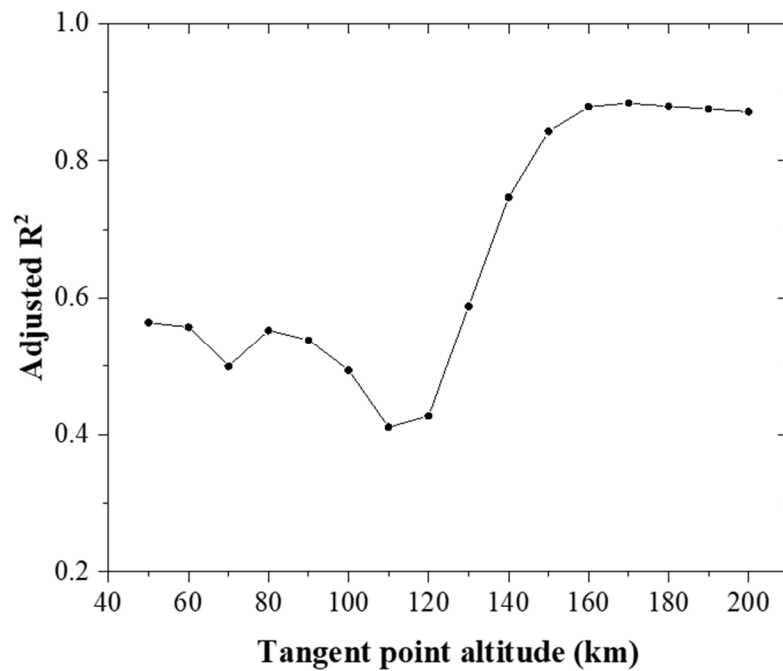


Figure 9. The adjusted R^2 of the fitting curves corresponding to different altitudes during 18–23 November 2003.

Based on the above figures, it can be observed that within the altitude range of 50–80 km, the correlation exhibits relative stability, ranging from 0.5 to 0.6, with minimal variation. Nevertheless, the correlation steadily decreases within the range of 80–110 km, reaching its lowest value of 0.41 at 110 km. This can be attributed to the complexity of photochemical reactions occurring around the altitude of 110 km, as the Dst index is derived from global station measurement data. Consequently, the Dst index is unable

to capture such fine details, leading to a diminished correlation at an altitude around 110 km. Subsequently, the correlation progressively rises with increasing altitude, reaching its peak of 0.88 at 170 km, denoting the strongest correlation. This high correlation is maintained within the altitude range of 160–200 km, with values around 0.87. Considering these findings, for this particular auroral disturbance event, the NO 5.3 μm radiance at the altitude of 170 km exhibits the strongest correlation with the Dst index ($R^2_{\text{adj}} = 0.88$). The relationship between the two can be represented by the following equation:

$$\text{Rad} = (-2.26232e - 06) * \text{Dst} - (2.26337e - 05) \quad (9)$$

Although Equation (9) presented here only applies to the results at 55°S 160°W, 170 km point for this particular aurora event, the high correlation coefficient of 0.88 indicates the feasibility of establishing a parameterized formula between the Dst index and the NO 5.3 μm radiance. This relationship has significant implications for future research on predicting the intensity range of the NO 5.3 μm emission in auroras using the Dst index.

4. Conclusions

The TIMED/SABER-observed NO 5.3 μm infrared radiation is studied during two consecutive auroral events, with the Dst index reaching a minimum value of -422 nT in 18–23 November 2003. Then, this period was chosen for the analysis of the spatiotemporal variations in NO 5.3 μm radiance. The time series of NO 5.3 μm radiance was analyzed at 55°N 160°W considering different altitudes. The altitude range was then divided into four groups for statistical analysis. The radiance value within the altitude range of 100–150 km showed the most significant response to auroral disturbances, reaching a maximum value of 3.38×10^{-3} W/m²/sr at 123 km of altitude. This value was approximately 10 times higher than the average radiance value during quiet periods. Moreover, the radiance value remained consistently high for almost 40 h primarily at an altitude of approximately 120–130 km. As the first disturbance recovered, the radiation value entered a recovery phase. However, at 18:00 UT on 22 November, a sudden increase in NO 5.3 μm radiance occurred around 120 km altitude. This increase expanded over a range of approximately ± 20 km due to the second aurora. Although not as intense as the first one, the radiance value reached 9.85×10^{-4} W/m²/sr by 13:00 UT on 23 November, which was 7 times higher than the average value during quiet periods. Subsequently, the time series of radiance at the tangent point of 120 km between the latitude 51°S–83°N and longitude 60°W–160°W was analyzed. The differences between the northern and southern hemispheres during the “recovery process” of the NO 5.3 μm radiance value were observed, with the recovery process starting earlier in the northern hemisphere. In the subsequent statistical analysis, the minimum radiation value remained relatively constant throughout the entire disturbance process, reflecting spatial and temperature limitations in the auroral excitation process. However, the maximum value and degree of variation altered significantly. Finally, the correlation between the NO 5.3 μm radiance value at 120 km and temperature, solar wind speed, AE index, and Dst index were analyzed. Only the correlation with the Dst index showed significance, with an R^2_{adj} value of 0.42. Subsequently, the correlation between the Dst index and the NO 5.3 μm radiance (with a 10 km interval) within 50–200 km was analyzed, indicating the highest correlation with the radiance at 170 km ($R^2_{\text{adj}} = 0.88$).

5. Discussion

As is known, strong geomagnetic disturbances have adverse effects on aerospace activities. For satellites carrying out missions during auroral disturbances, the enhancement of infrared background radiance within the field of view reduces the contrast of target signals, causing interference in target identification processes. Additionally, satellite laser communication systems commonly exploit infrared light for data transmission due to their superior penetration capability and faster data transfer rates. Nevertheless, as communication links traverse the atmosphere, the heightened infrared background radiation induced by auroral

disturbances may compromise signal-to-noise ratios, consequently deteriorating communication quality [55]. It is evident from the foregoing conclusions that the amplification of atmospheric limb infrared background radiation due to auroral disturbances reached approximately one order of magnitude. Hence, it is imperative to conduct a quantitative examination of NO 5.3 μm infrared radiation variations during auroral periods, serving as an early warning metric to mitigate the impact on target identification and enhance the resilience of communication links against interference. The correlation analysis between these radiance variations and the Dst index furnishes data support for the subsequent modeling of NO 5.3 μm infrared radiation fluctuations during auroral periods.

Author Contributions: Conceptualization, H.W. and C.D.; methodology, H.W., C.D. and F.W.; software, C.D. and F.W.; validation, F.W., S.C. and W.L.; formal analysis, S.C.; investigation, F.W. and C.Z.; resources, F.W.; data curation, F.W. and C.Z.; writing—original draft preparation, F.W.; writing—review and editing, H.W., C.D. and W.L.; visualization, F.W. and S.C.; supervision, C.D.; project administration, H.W. and C.D.; funding acquisition, H.W. and C.D. All authors have read and agreed to the published version of the manuscript.

Funding: This research was funded by the National Key Research and Development Program of China, grant number 2019YFA0706004.

Data Availability Statement: The raw data supporting the conclusions of this article will be made available by the authors on request.

Acknowledgments: We thank the OMNI (https://omniweb.gsfc.nasa.gov/html/ow_data.html) and TIMED/SABER (<https://saber.gats-inc.com>) scientific teams for providing the solar–terrestrial space environmental parameters and radiance data used in this paper. We all thank the funding support provided by the National Key Research and Development Program of China (2019YFA0706004).

Conflicts of Interest: The authors declare no conflicts of interest.

References

1. Liu, Z. *Space Physics*; Harbin Institute of Technology Press: Harbin, China, 2005.
2. Liu, Z. Solar-terrestrial space environment and its influence on economic activities. In *Chinese Geophysical Society, Proceedings of the 12th Annual Conference of the Chinese Geophysical Society*; China Building Materials Industry Press: Beijing, China, 1996.
3. Wang, C.; Chen, Z.; Hu, L.; Hu, Z.; Xue, X.; Xu, Q.; Zhang, X.; Li, F.; Wang, W.; Zong, W.; et al. Development and prospect of China's space-based and ground-based space environment monitoring platforms. *Spacecr. Environ. Eng.* **2021**, *38*, 225–239.
4. Cliver, E.W.; Svalgaard, L. The 1859 Solar–Terrestrial Disturbance And the Current Limits of Extreme Space Weather Activity. *Sol. Phys.* **2004**, *224*, 407–422. [[CrossRef](#)]
5. Fang, T.W.; Kubaryk, A.; Goldstein, D.; Li, Z.; Fuller Rowell, T.; Millward, G.; Singer, H.J.; Steenburgh, R.; Westerman, S.; Babcock, E. Space Weather Environment during the SpaceX Starlink Satellite Loss in February 2022. *Space Weather* **2022**, *20*, e2022SW003193. [[CrossRef](#)]
6. Chappell, C.R. The terrestrial plasma source: A new perspective in solar-terrestrial processes from Dynamics Explorer. *Rev. Geophys.* **1988**, *26*, 229–248. [[CrossRef](#)]
7. Gonza Lez-Esparza, J.A.; Cuevas-Cardona, M.C. Observations of low-latitude red Aurora in Mexico during the 1859 Carrington geomagnetic storm. *Space Weather* **2018**, *16*, 593–600. [[CrossRef](#)]
8. Silverman, S.M.S.V. Low-latitude auroras: The great aurora of 4 February 1872. *J. Atmos. Sol.-Terr. Phy.* **2008**, *70*, 1301–1308. [[CrossRef](#)]
9. Wu, Y. Energy Deposition of Aurora and Non-Equilibrium Infrared Radiation. Master's Thesis, Harbin Institute of Technology, Harbin, China, 2013.
10. Winick, J.R.; Picard, R.H.; Joseph, R.A.; Sharma, R.D.; Wintersteiner, P.P. *Infrared Spectral Radiance Code for the Auroral Thermosphere (AARC)*; Transactions of the American Clinical & Climatological Association: Baltimore, MD, USA, 1987.
11. Bermejo-Pantaleón, D.; Funke, B.; López-Puertas, M.; García-Comas, M.; Stiller, G.P.; von Clarmann, T.; Linden, A.; Grabowski, U.; Höpfner, M.; Kiefer, M.; et al. Global observations of thermospheric temperature and nitric oxide from MIPAS spectra at 5.3 μm . *J. Geophys. Res. Space Phys.* **2011**, *116*. [[CrossRef](#)]
12. Bharti, G.; Krishna, M.V.S.; Bag, T.; Jain, P. Storm Time Variation of Radiative Cooling by Nitric Oxide as Observed by TIMED-SABER and GUVI. *J. Geophys. Res. Space Phys. Sect.* **2018**, *123*, 1500–1514. [[CrossRef](#)]
13. Gardner, J.L.; Puertas, M.L.; Funke, B.; Miller, S.M.; Lipson, S.J.; Sharma, R.D. Rotational and spin-orbit distributions of NO observed by MIPAS/ENVISAT during the solar storm of October/November 2003. *J. Geophys. Res. Space Phys.* **2005**, *110*, A9S–A34S. [[CrossRef](#)]

14. Mlynczak, M.; Martin-Torres, F.J.; Russell, J.; Beaumont, K.; Jacobson, S.; Kozyra, J.; Lopez-Puertas, M.; Funke, B.; Mertens, C.; Gordley, L.; et al. The natural thermostat of nitric oxide emission at 5.3 μm in the thermosphere observed during the solar storms of April 2002. *Geophys. Res. Lett.* **2003**, *30*. [[CrossRef](#)]
15. Mlynczak, M.G.; Martin-Torres, F.J.; Crowley, G.; Kratz, D.P.; Funke, B.; Lu, G.; Lopez-Puertas, M.; Russell, J.M.R., III; Kozyra, J.; Mertens, C.; et al. Energy transport in the thermosphere during the solar storms of April 2002. *J. Geophys. Res. Space Phys.* **2005**, *110*; Erratum in *J. Geophys. Res. Space Phys.* **2007**, *112*, A2303. [[CrossRef](#)]
16. Barth, C.A. Reference models for thermospheric nitric oxide, 1994. *Adv. Space Res. Off. J. Comm. Space Res. (COSPAR)* **1996**, *18*, 103–115. [[CrossRef](#)]
17. Siskind, D.E.; Barth, C.A.; Roble, R.G. The response of thermospheric nitric oxide to an auroral storm: 1. Low and middle latitudes. *J. Geophys. Res.* **1989**, *94*, 16885–16898.
18. Cravens, T.E. The global distribution of nitric oxide at 200 km. *J. Geophys. Res.* **1981**, *86*, 5710–5714. [[CrossRef](#)]
19. Barth, C.A.; Mankoff, K.D.; Bailey, S.M.; Solomon, S.C. Global observations of nitric oxide in the thermosphere. *J. Geophys. Res. Space Phys.* **2003**, *108*. [[CrossRef](#)]
20. Siskind, D.E.; Barth, C.A.; Cleary, D.D. The possible effect of solar soft X rays on thermospheric nitric oxide. *J. Geophys. Res. Atmos.* **1990**, *95*, 4311–4317.
21. Barth, C.A. Comparison of a thermospheric photochemical model with Student Nitric Oxide Explorer (SNOE) observations of nitric oxide. *J. Geophys. Res. Space Phys.* **2004**, *109*. [[CrossRef](#)]
22. Lei, J.; Burns, A.G.; Thayer, J.P.; Wang, W.; Mlynczak, M.G.; Hunt, L.A.; Dou, X.; Sutton, E. Overcooling in the upper thermosphere during the recovery phase of the 2003 October storms. *J. Geophys. Res.* **2012**, *117*. [[CrossRef](#)]
23. Mlynczak, M.G.; Hunt, L.A.; Marshall, B.T.; Martin-Torres, F.J.; Mertens, C.J.; Russell, J.M.R., III; Remsberg, E.E.; López-Puertas, M.; Picard, R.; Winick, J.; et al. Observations of infrared radiative cooling in the thermosphere on daily to multiyear timescales from the TIMED/SABER instrument. *J. Geophys. Res. Space Phys.* **2010**, *115*. [[CrossRef](#)]
24. Mlynczak, M.G.; Hunt, L.A.; Marshall, B.T.; Iii, J.M.R.; Mertens, C.J.; Thompson, R.E.; Gordley, L.L. A combined solar and geomagnetic index for thermospheric climate. *Geophys. Res. Lett.* **2015**, *42*, 3677–3682. [[CrossRef](#)]
25. O’Neil, R.R.; Winick, J.R.; Picard, R.H.; Kendra, M. Auroral NO^+ 4.3 μm emission observed from the Midcourse Space Experiment: Multiplatform observations of 9 February 1997. *J. Geophys. Res. Space Phys.* **2007**, *112*. [[CrossRef](#)]
26. Sharma, R.D.; O’Neil, R.; Gardiner, H.; Gibson, J.; Dothe, H.; Duff, J.W.; Wintersteiner, P.P.; Kendra, M. Midcourse Space Experiment: Auroral enhancement of nitric oxide medium-wave infrared emission observed by the Spatial Infrared Imaging Telescope III radiometer. *J. Geophys. Res. Space Phys.* **2001**, *106*, 21351–21365. [[CrossRef](#)]
27. Adler-Golden, S.M.; Matthew, M.W.; Smith, D.R. Upper Atmospheric Infrared Radiance from CO_2 and NO Observed during the SPIRIT 1 Rocket Experiment. *J. Geophys. Res. Space Phys.* **1991**, *96*, 11319–11329. [[CrossRef](#)]
28. Espy, P.J.; Harris, C.R.; Steed, A.J.; Straka, J.C.U.A. Rocketborne interferometer measurement of infrared auroral spectra. *Planet. Space Sci.* **1988**, *36*, 543–551. [[CrossRef](#)]
29. Kockarts, G. Nitric oxide cooling in the terrestrial thermosphere. *Geophys. Res. Lett.* **1980**, *7*, 137–140. [[CrossRef](#)]
30. Sharma, R.D.; Dothe, H.; von Esse, F. On the rotational distribution of the 5.3 μm “thermal” emission from nitric oxide in the nighttime terrestrial thermosphere. *J. Geophys. Res. Space Phys.* **1996**, *101*, 17129–17135. [[CrossRef](#)]
31. Murphy, R.E.; Lee, E.T.P.; Hart, A.M. Quenching of vibrationally excited nitric oxide by molecular oxygen and nitrogen. *J. Chem. Phys.* **1975**, *63*, 2919. [[CrossRef](#)]
32. Gardner, J.L.; Funke, B.; Mlynczak, M.G.; López-Puertas, M.; Martin-Torres, F.J.; Russell, J.M.R., III; Miller, S.M.; Sharma, R.D.; Winick, J.R. Comparison of nighttime nitric oxide 5.3 μm emissions in the thermosphere measured by MIPAS and SABER. *J. Geophys. Res. Space Phys.* **2007**, *112*. [[CrossRef](#)]
33. Hwang, E.; Castle, K.J.; Dodd, J.A. Vibrational relaxation of $\text{NO}(v = 1)$ by oxygen atoms between 295 and 825 K. *J. Geophys. Res. Space Phys.* **2003**, *108*. [[CrossRef](#)]
34. Vitt, F.M.; Cravens, T.E.; Jackman, C.H. A two-dimensional model of thermospheric nitric oxide sources and their contributions to the middle atmospheric chemical balance. *J. Atmos. Sol.-Terr. Phys.* **2000**, *62*, 653–667. [[CrossRef](#)]
35. Barth, C.A. Nitric oxide in the lower thermosphere. *Planet. Space Sci.* **1992**, *40*, 315–336. [[CrossRef](#)]
36. Bag, T.; Li, Z.; Rout, D. SABER Observation of Storm-Time Hemispheric Asymmetry in Nitric Oxide Radiative Emission. *J. Geophys. Res. Space Phys.* **2021**, *126*. [[CrossRef](#)]
37. Li, Z.; Knipp, D.; Wang, W. Understanding the Behaviors of Thermospheric Nitric Oxide Cooling during the 15 May 2005 Geomagnetic Storm. *J. Geophys. Res. Space Phys. Sect.* **2019**, *124*, 2113–2126. [[CrossRef](#)]
38. Bag, T.; Rout, D.; Ogawa, Y.; Singh, V. Thermospheric NO Cooling during an Unusual Geomagnetic Storm of 21–22 January 2005: A Comparative Study between TIMED/SABER Measurements and TIEGCM Simulations. *Atmosphere* **2023**, *14*, 556. [[CrossRef](#)]
39. Thatcher, L.J.; Müller, H.R. Statistical investigation of hourly OMNI solar wind data. *J. Geophys. Res.* **2011**, *116*. [[CrossRef](#)]
40. Vokhmyanin, M.V.; Stepanov, N.A.; Sergeev, V.A. On the Evaluation of Data Quality in the OMNI Interplanetary Magnetic Field Database. *Space Weather* **2019**, *17*, 476–486. [[CrossRef](#)]
41. Papitashvili, N.; Bilitza, D.; King, J. OMNI: A description of near-Earth solar wind environment. In Proceedings of the 40th COSPAR Scientific Assem, Moscow, Russia, 2–10 August 2014.
42. Troshichev, O.A.A.O.; Sormakov, D.A.A. PC index as a proxy of the solar wind energy that entered into the magnetosphere: (5) verification of the solar wind parameters presented at OMNI website. *J. Atmos. Sol. Terr. Phys.* **2019**, *196*, 105147. [[CrossRef](#)]

43. Papitashvili, N.E.; King, J.H. A draft high resolution OMNI data set. In *AGU Spring Meeting Abstracts*; 2006. Available online: <https://ui.adsabs.harvard.edu/abs/2006AGUSMSM33A..02P/abstract> (accessed on 14 April 2024).
44. Russell, J.M.I.; Mlynczak, M.G.; Gordley, L.L.; Tansock, J.J., Jr.; Esplin, R.W. Overview of the SABER experiment and preliminary calibration results. *Proc. SPIE-Int. Soc. Opt. Eng.* **1999**, *3756*, 277–288.
45. Mertens, C.J.C.J.; Russell, J.M.J.R., III; Mlynczak, M.G.M.G.; She, C.J.L.C.; Schmidlin, F.J.F.O.; Goldberg, R.A.R.A.; López-Puertas, M.P.I.E.; Wintersteiner, P.P.W.A.; Picard, R.H.R.P.; Winick, J.R.J.W.; et al. Kinetic temperature and carbon dioxide from broadband infrared limb emission measurements taken from the TIMED/SABER instrument. *Adv. Space Res.* **2009**, *43*, 15–27. [[CrossRef](#)]
46. Xu, J.; She, C.Y.; Yuan, W.; Mertens, C.; Mlynczak, M.; Russell, J. Comparison between the temperature measurements by TIMED/SABER and lidar in the midlatitude. *J. Geophys. Res. Space Phys.* **2006**, *111*. [[CrossRef](#)]
47. Bharti, G.; Krishna, M.V.S.; Singh, V. Radiative cooling due to NO at 5.3 μm emission as observed by TIMED/SABER over Asian sector. *Adv. Space Res.* **2019**, *64*, 1989–2001. [[CrossRef](#)]
48. Jiang, G.; Wang, W.; Xu, J.; Yue, J.; Burns, A.G.; Lei, J.; Mlynczak, M.G.; Russell, J.M. Responses of the lower thermospheric temperature to the 9-day and 13.5-day oscillations of recurrent geomagnetic activity. *J. Geophys. Res. Space Phys.* **2014**, *119*, 4841–4859. [[CrossRef](#)]
49. Russell, J.M., III; Mlynczak, M.G.; Gordley, L.L. Overview of the Sounding of the Atmosphere Using Broadband Emission Radiometry (SABER) experiment for the Thermosphere-Ionsphere-Mesosphere Energetics and Dynamics (TIMED) mission. *Opt. Spectrosc. Tech. Instrum. Atmos. Space Res.* **1994**, *2266*, 406–415.
50. Mlynczak, M.G.; Hunt, L.A.; Lopez-Puertas, M.; Funke, B.; Emmert, J.; Solomon, S.; Yue, J.; Russell, J.M.; Mertens, C. Spectroscopy, gas kinetics, and opacity of thermospheric nitric oxide and implications for analysis of SABER infrared emission measurements at 5.3 μm . *J. Quant. Spectrosc. Radiat.* **2021**, *268*, 107609. [[CrossRef](#)]
51. Davis, T.N.; Sugiura, M. Auroral electrojet activity index AE and its universal time variations. *J. Geophys. Res.* **1966**, *71*, 785–801. [[CrossRef](#)]
52. Sharma, R.D.; Dothe, H.; von Esse, F.; Kharchenko, V.A.; Sun, Y.; Dalgarno, A. Production of vibrationally and rotationally excited NO in the night time terrestrial thermosphere. *J. Geophys. Res. Space Phys.* **1996**, *101*, 19707–19713.
53. Armstrong, P.S.; Lipson, S.J.; Dodd, J.A.; Lowell, J.R.; Blumberg, W.A.M.; Nadile, R.M. Highly rotationally excited NO (v, J) in the thermosphere from CIRRIS 1A limb radiance measurements. *Geophys. Res. Lett.* **1994**, *21*, 2425–2428. [[CrossRef](#)]
54. Crowley, G.; Ridley, A.; Winningham, D.; Frahm, R.; Sharber, J.; Russell, J.I. On the hemispheric symmetry in thermospheric nitric oxide. *Geophys. Res. Lett.* **1999**, *26*, 1545–1548. [[CrossRef](#)]
55. Jiajia, Y.; Fangfang, Z.; Lishan, C.; Ji, Z. Infrared Characteristics of Ground Targets and Background Observed from NearSpace. *Infrared Technol.* **2021**, *43*, 670–678.

Disclaimer/Publisher’s Note: The statements, opinions and data contained in all publications are solely those of the individual author(s) and contributor(s) and not of MDPI and/or the editor(s). MDPI and/or the editor(s) disclaim responsibility for any injury to people or property resulting from any ideas, methods, instructions or products referred to in the content.